PCCP

Accepted Manuscript

ROYAL SOCIETY OF CHEMISTRY

www.rsc.org/pccp

Physical Chemistry Chemical Physics RSCPublishing

ARTICLE

Hierarchical $NiMoO_4$ nanowire arrays supported on macroporous graphene foam as binder-free 3D anodes for high-performance lithium storage

Cite this: DOI: 10.1039/x0xx00000x

Received 00th January 2012,
Accepted 00th January 2012

DOI: 10.1039/x0xx00000x

www.rsc.org/

Bo Wang, Songmei Li,* Xiaoyu Wu, Jianhua Liu, and Wenming Tian

A novel three-dimensional (3D) $NiMoO_4$ nanowire arrays (NWAs) grown directly onto the surface of the macroporous graphene foams (GF) with robust adhesion were synthesized via a facile chemical vapor deposition (CVD) and subsequent hydrothermal route. The as-prepared $NiMoO_4$ nanowires composed of ultra-small nanoparticles (~5 nm) with diameter of 70-150 nm and several micrometers in length. Such as-grown $NiMoO_4$ NWAs/3DGF composites are then evaluated as monolithic electrodes for lithium-ion batteries (LIBs) without the need of binders or metal-based current collectors. Benefitting from the unique three-dimensional arrayed architecture and characteristics with a high specific surface area and more active sites which facilitate fast electron and ionic transport within the electrode, the $NiMoO_4$ NWAs/GF composites deliver a high reversible specific capacity of 1088.02 mAh g^{-1} at a current density of 200 mA g^{-1} and 867.86 mAh g^{-1} after 150 cycles (79.77% retention of the second cycle), and excellent rate capability. With the advantages of excellent electrochemical performance and facile synthesis method, the $NiMoO_4$ nanowire arrays supported on 3DGF exhibit great potential as an anode material for LIBs.

Introduction

Rechargeable lithium-ion batteries (LIBs) are widely recognized as the choice of power sources for a wide range of applications, such as portable electronic devices, electrical/hybrid vehicles, implantable medical devices and storage devices of renewable energy.[1-3] However, current commercial graphite anodes with limited specific capacity (372 mAh g^{-1}) and low power density give rise to a very limited energy output for LIBs.[4,5] Therefore, considerable efforts have been dedicated to explore alternative anode materials based on alloying or conversion reactions with higher reversibilitiy and rate capacities, as well as long-term cyclic stability.[6-8]

Transition metal molybdates, such as cobalt molybdates and nickel molybdates have been considered the promising candidates because the transition-metal centers for most of them possess multiple accessible valence states, which would enable a variety of reversible redox activity and reversibility, and thus generate high lithium storage properties for LIBs.[9-11] Particularly, their mixed-oxide forms exhibit far better electrochemical performance than monometallic component oxides due to the enhanced electrochemical reversibility and conductivity.[12-14] Despite these distinct advantages, transition metal oxides still suffer from kinetic problems derived from their intrinsic low electrical conductivity and slow solid-state diffusion of Li ions, as well as the concomitant volume expansion/contraction caused pulverization of electrode materials, which significantly limits its practical application in high performance LIBs.[15-16] Until now, the reported transition metal molybdates-based electrodes have been usually made by a traditional slurry-coating technique, where the involved binder has greatly decreased the electrical conductivity of the active materials, hindering the fast electron transport required by excellent cycling ability and rate capability.[10-11,15] In addition to alternative electrode materials, the rational design and fabricate of binder-free electrode architectures is also regarded as effective strategy to improve the performance for LIBs.

As an important class of nanostructures, self-supported nanowire arrays architecture grown directly on the conducting substrates has become a very promising material for nano-devices and very large-scale integrated circuits manufacturing.[17,18] Such an additive/binder-free electrode architectures can avoid the "dead surface" in traditional slurry-derived electrodes, which eliminates the need for binders and conducting additive, and then increases the

Key Laboratory of Aerospace Advanced Materials and Performance of Ministry of Education, School of Materials Science and Engineering, Beihang University, Beijing, 100191, China.

E-mail: songmei_li@buaa.edu.cn; Fax: +86-10-82317103; Tel: +86-10-82317103

Electronic supplementary information (ESI) available. See DOI:

mass energy density of the batteries.[19-21] Moreover, the self-supported nanowire arrays architecture provides numerous conducting channels for electron transport to the current collector, which benefit for high efficiency of ion and electron transports in the electrodes and across the electrode/electrolyte interface, therefore improving the lithium storage performance potentially.[22,23]

For various conductive substrates, especially 3D graphene foam (GF) assembled by two-dimensional (2D) graphene nanosheets exhibit continuously interconnected macroporous structures, low mass density, high specific surface area, excellent electrical conductivity, which can serve as robust matrix for loading electroactive materials for improving electrochemical performance of the electrode materials.[24,25] The 3D graphene matrices not only provide a conductive network for fast ion and electron transport, increase the electrolyte/electrode contact area, and maximize the utilization of active materials, but also can act as a volume buffer to absorb the internal stress due to the combination of 3D porous structures and the excellent intrinsic properties of graphene.[26,27] Recently, using porous Ni foam as a template in the CVD process is an effective way to produce seamless 3DGF with high conductivity comparable to other 3D carbonaceous materials, which would facilitate the fast mass and electron transport between the active materials and current collectors in electrochemical energy storage.[28-30]

Herein, we demonstrate a simple approach to fabricate 3D hierarchical $NiMoO_4$ nanowire arrays directly grown on a graphene foam (denoted as $NiMoO_4$ NWAs/3DGF) via a simple chemical vapor deposition (CVD) and subsequent hydrothermal route. The nanowires are composed of ultra-small nanoparticles (～5 nm) and further self-assembled into a hierarchical structure. When applied directly as anode for LIBs without any binders and conductive additives, the $NiMoO_4$ NWAs/3DGF electrode exhibited high lithium-storage capacity and impressive rate capability due to the unique hierarchical nanowire arrays and macroporous architecture with high electrolyte/electrode contact area, fast ion and electron transfer, and good strain accommodation.

Experimental

Synthesis of $NiMoO_4$ NWAs/GF composites

Growth of the 3DGF: Nickel foams (NF, Changsha Lyrun New Material Co., Ltd, China) with an areal density of ~0.038g cm^{-1} and a porosity of ~97.3% were used as 3D templates for the growth of GF by chemical vapor deposition (CVD). Briefly, prior to deposition, nickel foam cut into piece with the size of 2 cm×4 cm was degreased with acetone, etched with 1M HCl solution for 10 min, then washed by deionized water and ethanol for 10 min with sonication, respectively. After dried with nitrogen gas, the nickel foams were placed in the center of a quartz tube in a horizontal tube furnace (OTF-1200X), and samples were heated to 1050 ℃ in 50 min under an Ar (50 sccm.) and H_2 (20 sccm.) flow. The temperature was maintained for 30 min to reduce the formation of oxides on the surface of the nickel foams. A CH_4 gas (5 sccm.) was then flowed for 120 min with the same amounts of Ar and H_2. Following the synthesis, the CH_4 gas was turned off and the samples were rapidly cooled to room temperature under a constant flow of Ar (50 sccm.) and H_2 (20 sccm.). After the growth, the resulting graphene@Ni foam structure was etched in 2M $Fe(NO_3)_3$ solution at 80℃ for 12 hours to dissolve the nickel framework. Finally, free-standing 3DGF was obtained after washed with DI water and alcohol.

Synthesis $NiMoO_4$ NWAs/GF composites: The $NiMoO_4$ NWAs/GF composites were synthesized via a facile hydrothermal approach and the subsequent thermal annealing in Ar atmosphere. In a typical experiment, 3 mmol of $NiCl_2 \cdot 6H_2O$ and 3 mmol of $Na_2MoO_4 \cdot 7H_2O$ were dissolved successively in 90 mL deionized water with magnetic stirring at room temperature. After 10 min, the homogeneous solution was transferred to a 100 mL Teflon-lined autoclave with two pieces of the as-prepared 3DGF immersed into the reaction solution. The autoclave was sealed and maintained at 150 ℃ for 6 h, and then cooled down to room temperature. The NiMo-precursors grown on 3DGF was removed, rinsed with distilled water several times, and dried in air at 60 ℃. Finally, the NiMo-precursors/3DGF composites further annealed under the protection of argon gas at 300℃ for 2 h to obtain the $NiMoO_4$ NWAs/GF composites. For the comparison, $NiMoO_4$ nanowires powders were prepared by the same process only without adding the substrate of graphene foam.

Characterization

The phase composition and crystallographic structures of the samples were directly examined by using X-ray diffraction system (XRD, Rigaku D/max 2200PC) with Cu Kα radiation (λ=0.15418 nm). Morphology and crystalline structure of the samples were characterized with a JEOL JSM-7500F field-emission scanning electron microscope (SEM) and a JEOL JEM-2100F transmission electron microscope (TEM). For the TEM observations, the $NiMoO_4$ NWAs/3DGF composites were subjected to strong ultrasonication to detach the $NiMoO_4$ nanowires from the GF. The surface elemental composition analysis of the samples was performed by a JEOL JSM-7500F with energy dispersive X-ray spectroscopy (EDS) attachment. The specific surface area was determined by measuring N_2 adsorption-desorption isotherms using a an ASAP-2010 surface area analyzer at 77 K.

Electrochemical Measurements

The CR2025-type coin cells were assembled in an Ar-filled glovebox, in which oxygen and water contents were less than 1 ppm. The as-prepared $NiMoO_4$ NWAs/GF composites were punched in the form of 12 mm diameter disks, and then used directly as the working electrode without any conductive additive or polymer binders. In order to reduce the mass uncertainty of the electrodes, the as-prepared 3DGF and $NiMoO_4$ NWAs/3DGF composites were punched in the form of 12 mm diameter disks, and then used directly as the working electrode without any conductive additive and polymer binder. Then, we took 10 pieces of samples (3DGF and $NiMoO_4$ NWAs/3DGF composites, respectively) and weighed them together. The specific mass loading of the active material ($NiMoO_4$) for the testing electrodes was about ～1.0 mg cm^{-2}, estimated by weighing the graphene foam before and after the loading of $NiMoO_4$ NWAs. The metallic lithium circular foil was used as both the counter electrode and the reference electrode, a microporous

polypropylene membrane (Celgard 2400) served as the separator. The electrolyte consisted of 1 M $LiPF_6$ in ethylene carbonate (EC) and diethyl carbonate (DEC) (1:1 by volume). In a control experiment, the $NiMoO_4$ nanowires powder electrode were prepared by mixing 80 wt.% active material, 10 wt.% conducting carbon black, and 10 wt.% polyvinylidene fluoride binder in N-methyl-2-pyrrolidone. The homogeneous slurries were then pasted on copper current collector and dried under vacuum at 60 ℃ for 12 h. Before the electrochemical measurements, the assembled cells were aged in the glovebox for 10 h.

Galvanostatic charge-discharge and cyclic voltammetry (CV) measurements were conducted using a LAND CT2001A battery-testing instrument and a multichannel Arbin Instruments BT2000 (USA) unit in the voltage range of 0.005-3.0 V at room temperature (25±1℃). Electrochemical impedance spectroscopy (EIS) measurements were performed using a PARSTRAT 2273 electrochemical measurement system by employing an ac voltage of 5 mV amplitude in the frequency range from 100 kHz to 0.01 Hz.

Results and discussion

The fabrication process of the $NiMoO_4$ NWAs supported onto the skeleton of graphene foam is schematically depicted in Scheme 1. Two main steps are required for the entire fabrication process. Firstly, 3D macroporous graphene networks was grown on the scaffold of Ni foam via a chemical vapor deposition (CVD) method and then Ni skeleton was etched away by a $Fe(NO_3)_3$ solution to leave from the free-standing 3DGF. Secondly, the raw materials reacted under hydrothermal conditions and formed NiMo-precursors ($NiMoO_4$ xH_2O) grown directly onto the surface of graphene foam. And then the NiMo-precursors was thermally decomposed to $NiMoO_4$ nanowire arrays supported on the graphene foam under the protection of argon gas, which can be described by the simple dehydration reaction.

The crystallographic structure and phase purity of the samples were examined by powder X-ray diffraction (XRD). As shown in Fig. 1a, the XRD patterns of as-grown graphene foam show two significant diffraction peaks at 2θ = 26.5 and 54.6°, which were attributed to the (002) and (004) reflections of graphitic carbon (JCPDS 75-1621), respectively.[31,32] The sharp peak at 26.5 ° indicates high crystallinity and an interlayer space of ca. 0.34 nm. The high crystalline structure of graphene is favorable for the ion diffusion and electron transfer.[33] Apart from the characteristic peaks from graphene foam substrate, all other diffraction peaks originating from the $NiMoO_4$ NWAs/3DGF composites are well indexed to the standard XRD pattern of monoclinic $NiMoO_4$ (JCPDS Card no. 86-0361).[34,35] In order to preclude the strong impact of graphene foam substrate, the as-prepared $NiMoO_4$ nanowires powders in the same reaction system were also checked by XRD. As indicated in Fig. S1 (Supporting Information), the XRD pattern confirms that all the diffraction peaks are well matched with the standard pattern of monoclinic $NiMoO_4$ (JCPDS Card no. 86-0361).[36] Some weak peaks can be observed in the XRD patterns of $NiMoO_4$ NWAs/3DGF and $NiMoO_4$ nanowires powder, which could be attributed to the low crystallinity.

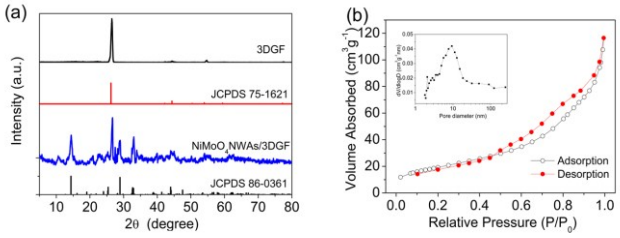

Fig. 1 (a) XRD patterns of the as-prepared 3DGF (black), $NiMoO_4$ NWAs/3DGF composites (blue), and the standard XRD pattern of monoclinic $NiMoO_4$. (b) Nitrogen adsorption-desorption isotherm of $NiMoO_4$ NWAs/3DGF composites and inset shows the corresponding BJH pore size distribution plots.

The pore nature of the products was characterized using N_2 adsorption-desorption measurements. Fig. 1b shows the nitrogen adsorption and desorption isotherms and the corresponding pore size distributions (inset) of $NiMoO_4$ NWAs/3DGF composites, respectively. As shown in Fig.1b, a typical type-IV isotherm characteristic with a distinct adsorption hysteresis loop in the P/P_0 range of 0.45-1.0, suggesting the existence of relatively large macropores and mesopores in the $NiMoO_4$ NWAs/3DGF composites. The mesopores mainly originate from the aggregation of primary

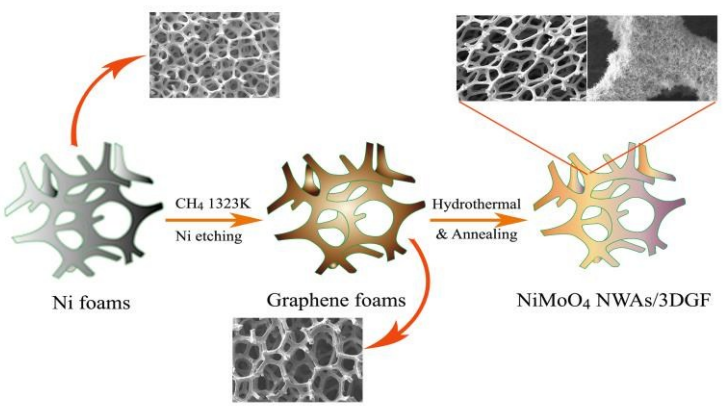

Scheme 1. Schematic representation of the fabrication process of $NiMoO_4$ NWAs onto skeleton of 3D macroporous graphene foam.

nanoparticles within a single $NiMoO_4$ nanowire, while the macropores and some of the large mesopores come from the void spaces between the $NiMoO_4$ nanowire and 3DGF. The specific surface areas were calculated from the Brunauer-Emmett-Teller (BET) method and the pore size distributions (PSD) were obtained by means of the Barrett-Joyner-Halenda (BJH) equation using the adsorption isotherm branch. The corresponding BET specific surface areas of $NiMoO_4$ NWAs/3DGF composites is calculated to be 70.83 m^2 g^{-1}. The pore size distribution curves of $NiMoO_4$ NWAs/3DGF composites is also shown in inset of Fig. 1b, and the average pore size in $NiMoO_4$ NWAs is in the range of 5-11 nm. The high specific surface area of $NiMoO_4$ NWAs/3DGF composites with massive mesopores and macropores, which is capable of providing sufficient electrode/electrolyte interfaces and increasing the number of reversible redox reaction sites, leads to high electrochemical capacity of the electrode material.[32]

The morphology and microstructure of the as-prepared samples were investigated by field-emission scanning electron microscopy (SEM). Fig. 2a shows the optical images of the as-prepared 3DGF and $NiMoO_4$ NWAs/3DGF composites. After removal of the Ni template, the color of the nickel foam changed from shiny white to dark gray (Fig. 2a) after the CVD process, suggesting the graphene sheets successfully replicates the 3D macroporous network structure of Ni foam without collapsing and cracking. It can be seen that the 3DGF surface completely turned into light green after the growth of $NiMoO_4$

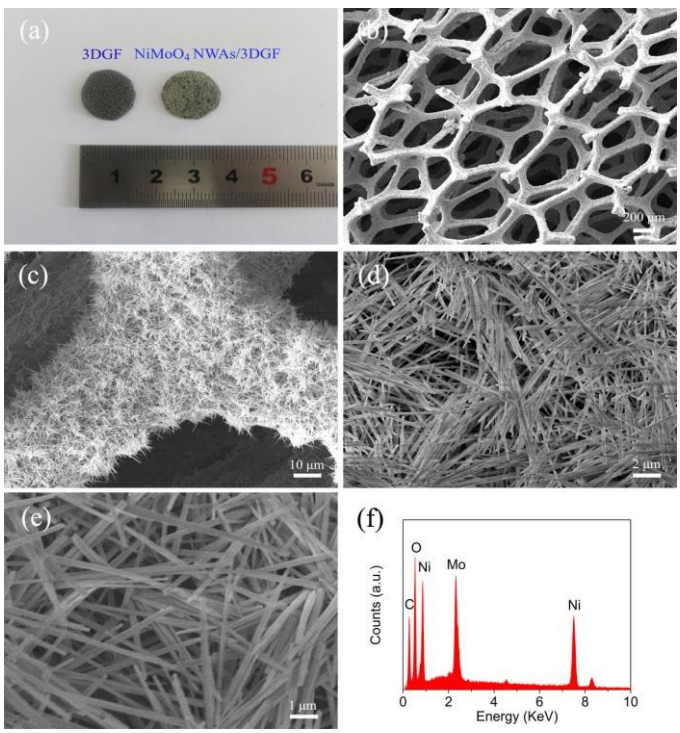

Fig. 2 (a) Digital image and (b-e) Typical SEM images of the $NiMoO_4$ NWAs grown on the surface of the 3DGF skeleton at different magnifications. and (h) EDS spectrum of the as-synthesized $NiMoO_4$@3DGF composites.

NWAs. As shown in Fig. S2a and b, the intact 3D network structure and smooth graphene skeleton with continuous macropores of hundreds of micrometers are clearly observed. The intrinsic grains and wrinkles of graphene sheets were well remained without any observable crack or break, indicating a continuous network of graphene. SEM images in Fig. S2d show that the foams are built from corrugated hollow micro-tubes to form a 3D interconnected architecture. It can be seen that the graphene micro-tube is in diameters of 30-50 μm, with thin layer graphene sheet as the wall of the micro-tube. Furthermore, it can be observed that the inner wall of graphene micro-tube seems flat, while the outside surface of the graphene micro-tube is rugged, which is consistent with the observations of Fig . S2c. Fig. 2b-e show the typical SEM images of the $NiMoO_4$ nanowires supported on 3DGF at different magnifications. It can be seen that the surface of the GF was fully covered by the grass-like $NiMoO_4$ nanowires with lengths of several micrometers. From a closer view in Fig. 2c-e, the $NiMoO_4$ nanowires has a sharp tip and the diameter of the nanowire is in the range of 70 -150 nm. The composition of the as-prepared products was confirmed by EDS analysis. It is clear that there is no Ni element in the 3DGF, which indicates that nickel has been completely dissolved (Fig. S3 Supporting Information). As shown in Fig. 2f, the EDS spectrum verifies the composition of th $NiMoO_4$ NWAs/3DGF composites to be Ni, Mo, O and C elements, arising from the carbon substrate can be found in this spectrum. In strong contrast, in the absence of GF, the exact same synthesis process produced $NiMoO_4$ nanowires of about 100-300 nm in diameter (Fig. S4 Supporting Information), which is several two folds thicker and aggregate severely than the nanowires in the $NiMoO_4$ NWAs/3DGF composites. The $NiMoO_4$ nanowire arrays are densely grown on 3D macroporous graphene foam with highly open space between nanowires which facilitate the electrolyte penetration into the inner region of the electrode, increase the utilization of the active materials, and accommodate volume expansion upon Li insertion. Furthermore, the direct growing of nanowires can ensure good mechanical adhesion and electrical connection to the current collector, avoid the use of polymer binders and conducting additives which generally increase the series resistance and the deterioration of specific capacity during redox reactions.

Further insight into the detailed microstructure of the nanowire in $NiMoO_4$ NWAs/3DGF composites is demonstrated by TEM. Fig. 3a is a typical TEM image of an individual $NiMoO_4$ nanowire scraped off from graphene foam, confirming their needle-like nanostructures. The $NiMoO_4$ nanowires with diameter of 70-150 nm and length up to several micrometers can be seen clearly, which are in good agreement with the SEM observations. The high-resolution TEM (HRTEM) image of the middle region shown in Fig. 3b further reveals that the $NiMoO_4$ nanowire with a rough surface was composed of lots of crystalline $NiMoO_4$ nanoparticles with a size of ca. 5 nm. Besides, irregular pores with an average size of 5-11 nm are numerously disturbed in the $NiMoO_4$ nanowire. As reported in the literatures,[37] the crystal growth mechanism of "oriented attachment" and "self-assembly" could be proposed to demonstrate the complicated nano-architecture process. The oriented attachment mechanism describes the spontaneous self-organization

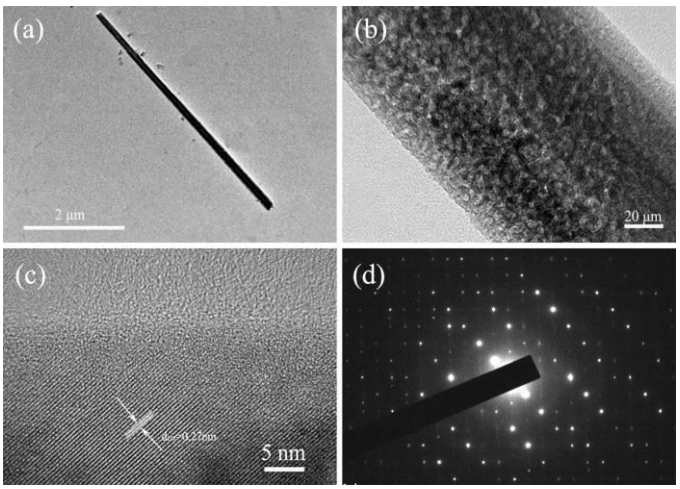

Fig. 3 (a,b) TEM, (c) HRTEM images, and (d) SAED pattern of the $NiMoO_4$ nanowires which were detached from GF by sonication and transferred on the TEM grid.

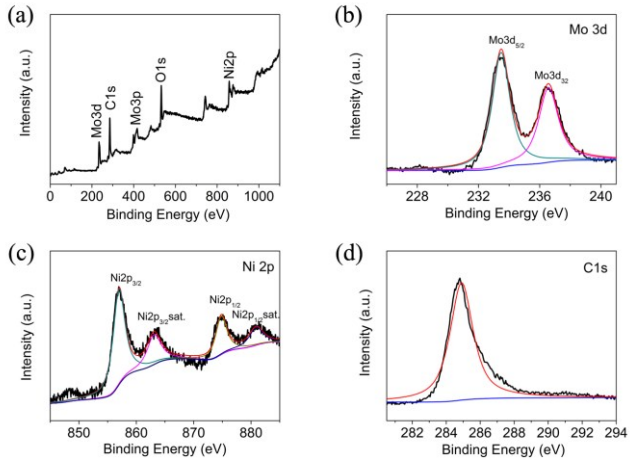

Fig. 4 The XPS spectra of the $NiMoO_4$ NWAs/3DGF composites. (a) The survey XPS spectrum, (b) the Mo 3d XPS spectrum, (c) the Ni 2p XPS spectrum and (d) the C XPS spectrum.

of adjacent particles, followed by the joining of these particles at a planar interface. The process is particularly relevant in the nanocrystalline regime, where bonding between the particles reduces overall energy by removing surface energy associated with unsatisfied bonds.[38] In addition, the formation of the mesopores probably results from the successive release and lose of water molecules during the thermal decomposition of the precursors.[39] The existence of pores in nanowires could benefit Li ion diffusion in the nanowires, provide larger contact areas with electrolyte, buffer the strain induced by the volume change, and enhance the electrochemical performance of the electrode. The high-resolution TEM (HRTEM) image in Fig. 3c reveals the interplanar spacing of 0.27 nm, corresponding to the (222) planes of $NiMoO_4$.[34,35] In addition, the selected-area electron diffraction (SAED) pattern of the $NiMoO_4$ nanowire (Fig. 3d) shows a well-defined lattice, indicating their crystalline characteristics.[40] The crystal growth mechanism of "oriented attachment" and "self-assembly" were proposed to demonstrate the complicated nano-architecture process.[37] In the our reaction, the 3DGF were used as the "substrate", which can guide the $NiMoO_4$ self-assembling growth in aqueous solution without surfactant and stabilizers. Then the "oriented attachment" can guide the nanoparticles oriented growth. Meanwhile, the similar phenomena can be commonly observed in $NiMoO_4$-based materials.[34,35]

To further investigate the elemental composition and valence state of the as-prepared $NiMoO_4$ NWAs/3DGF composites, X-ray photoelectron spectroscopy (XPS) measurements were carried out. Fig. 4a shows a typical survey XPS spectrum of the $NiMoO_4$ NWAs/3DGF composites, where the existing characteristic peaks correspond to Ni 2p, Mo 3d, C 1s, and O 1s confirm the presence of Ni, Mo, C and O elements within the as-prepared $NiMoO_4$ NWAs/3DGF composites, and no other impurities. By using a Gaussian fitting method, the binding energies of Mo $3d_{3/2}$ and Mo $3d_{5/2}$ peaks (Fig. 4b) are located at 233.5 eV and 236.6 eV can be observed in the region of Mo 3d, respectively. The binding energy and the splitting width (△Mo 3d = 3.1 eV) are characteristics of Mo^{6+} oxidation state in $NiMoO_4$@3DGF, which is in good agreement with those reported for Mo^{6+}.[41,42] The core level spectra of Ni 2p (Fig. 4c) show two major peaks at 856.9 and 874.6 eV, which can be assigned to Ni $2p_{3/2}$ and Ni $2p_{1/2}$, representative of the existence of the Ni^{2+}.[43,44] Fig. 4d represents the C 1s core level spectrum of the $NiMoO_4$@3DGF composites. The binding energy peak at 284.6 eV corresponds to sp^2 hybridized carbon.[45] The high-resolution spectrum of the O 1s region (Fig. S5 Supporting Information) shows the binding energy (O 1s) is 531.5 eV which corresponds to lattice oxygen.[46,47] The XPS results confirm that the valence of Ni, Mo and O elements are +2, +6 and -2, respectively.

To evaluate the electrochemical performance of $NiMoO_4$ NWAs/3DGF composites electrodes, a typical two electrode configuration was constructed. The $NiMoO_4$ NWAs/3DGF composites were served as electrodes as well as current collectors with binder-free, macroporous open pore structures and conductive framework which provides highly porous channels for the full access of electrolytes to active materials. The corresponding electrochemical performances of the $NiMoO_4$ NWAs/3DGF composites electrodes for lithium storage are shown in Fig. 5. Fig. 5a presents the initial five consecutive cyclic voltammogram (CV) curves of the $NiMoO_4$ NWAs/3DGF electrode at a scanning rate of 0.1 mV s^{-1} in the voltage window of 0.001-3.0 V. In the first cathodic scan, the two well-defined reduction peaks at around 0.58 V and 1.26 V can be corresponded to the irreversible electrochemical reduction of $NiMoO_4$ to metallic Mo and Ni, as well as the decomposition of organic electrolyte to form a solid-electrolyte interphase (SEI) layer at the electrode/electrolyte interphase.[10,48] Meanwhile, the two anodic peaks at around 1.34 and 1.68 V can be attributed to the oxidation of Ni to Ni^{2+} and Mo to Mo^{6+}, respectively. In the second and subsequent cycles, two cathodic peaks located at 0.58 V and 1.26 V are shifted to 0.61 and 1.40 V, which are induced by the reversible reductive reaction of MoO_3 and NiO to Mo and Ni metal, respectively. It is noteworthy that the peak intensity and integral areas are almost identical from the second cycle to the fifth cycle, suggesting the good reversibility and stable

performance of the electrode.[49,50] On the basis of the CV results and previous reports, the electrochemical reactions of $NiMoO_4$ NWAs/3DGF electrode involved during the charge-discharge processes can be described as follows:[15,51]

$$NiMoO_4 + 8Li^+ + 8e^- \rightarrow Ni + Mo + 4Li_2O \quad (1)$$

$$Ni + Li_2O \rightarrow NiO + 2Li^+ + 2e^- \quad (2)$$

$$Mo + 3Li_2O \rightarrow MoO_3 + 6Li^+ + 6e^- \quad (3)$$

$$Ni + Mo + 4Li_2O \leftrightarrow NiO + MoO_3 + 8Li^+ + 8e^- \quad (4)$$

Typical galvanostatic discharge-charge curves of the $NiMoO_4$ NWAs/3DGF electrode at a current density of 200 mA g^{-1} in the voltage range of 0.005-3.0 V vs. Li^+/Li. As shown in Fig. 5b, the initial specific discharge and charge capacities of the $NiMoO_4$ NWAs/3DGF electrode are 1308.29 and 1110.94 mAh g^{-1}, respectively. The specific discharge capacity in the second cycle is 1088.02 mAh g^{-1} and the capacity retention is 83.2%, which is still much higher than the theoretical capacity value based on the conversion reaction (4). The extra initial discharge capacity and irreversible capacity loss of 15.08% is attributed to the irreversible conversion reaction of $NiMoO_4$ with Li ions and inevitable formation of SEI layer by electrolyte decomposition and surface reaction on the active material in good agreement with the above CV results. The SEI layer is a gel-like film with complex components including organic layer and inorganic layer that is first formed at a low voltage (0.02-1.0 V) during the first discharge and covers the electrode.[52,53] Moreover, the columbic efficiency is rapidly increases from 84.92% in the first cycle to 98% in the second cycle and then remains above 99% during the subsequent cycles.

The cycle stability and rate capability of 3DGF supported $NiMoO_4$ NWAs electrode and conventional $NiMoO_4$ nanowires electrode were investigated by galvanostatic discharge and charge measurements with various applied currents. Fig. 5c compares the cycling performance of the $NiMoO_4$ NWAs/3DGF electrode with conventionally prepared electrode from casting $NiMoO_4$ nanowires based slurry on a copper current collector at a current density of 200 mA g^{-1} at room temperature. It can be seen that the $NiMoO_4$ NWAs/3DGF electrode show significantly improved capacities in comparison with the conventional $NiMoO_4$ nanowires electrode. The capacity of the conventional $NiMoO_4$ nanowires electrode drops rapidly to below 590 mAh g^{-1} after 40 cycles. In contrast, the $NiMoO_4$ NWAs/3DGF electrode shows superior cycling performance, delivering a high reversible capacity of 867.86 mAh g^{-1} after 150 cycles, which is about 79.77% of the reversible capacity in the second cycle. Compared to the conventional traditional slurry-coating electrode, the integrated and binder-free $NiMoO_4$ NWAs/3DGF electrodes not only avoid the use of a polymer binder and conductive additives in the preparation process of traditional slurry electrode, but also reduce the electron transfer distance and ion diffusion path obviously, and as a result, the reversible capacity especially high rate capacity can be improved.[36,] Meanwhile, the traditional slurry-derived electrode used for electrochemical evaluation seriously limits the reversibility of the electroactive $NiMoO_4$ because of the increased "dead surface".[51] Compared with other reported $NiMoO_4$-based materials, such as Nanocrystalline $NiMoO_4$ thin film (148 mAh g^{-1} after 40 cycles),[10] $Ni_xCo_{1-x}MoO_4$ nanowire (520 mAh g^{-1} at current density of 196 mA g^{-1} after 20 cycles),[11] and $NiMoO_4$ NSs/Ni foam (680 mAh g^{-1} after 150 cycles),[54] the $NiMoO_4$ NWAs/3DGF possess much higher capacities and better cyclability obviously.

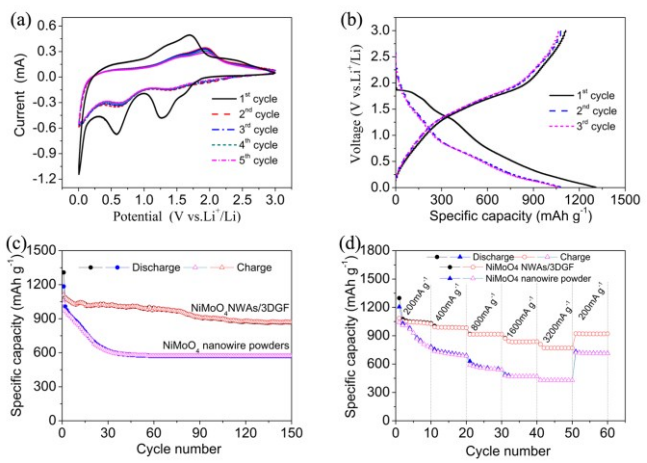

Fig. 5 (a) Cyclic voltammograms of the $NiMoO_4$ NWAs/3DGF electrode for the initial five cycles at a scan rate of 0.1 mV s^{-1} in the voltage range of 0.005-3.0 V, (b) Galvanostatic charge-discharge voltage profiles of $NiMoO_4$ NWAs/3DGF electrode for the first three cycles at a current density of 200 mA g^{-1}, (c) Comparison of the cycling performance of the $NiMoO_4$ NWAs/3DGF electrode with $NiMoO_4$ nanowires electrode at the current density of 200 mA g^{-1}, (d) Comparison of the rate performance of the $NiMoO_4$ NWAs/3DGF electrode with $NiMoO_4$ nanowires electrode.

The rate performance of LIB anodes is highly crucial especially for high-power applications in power grids and electric vehicles. To further investigate the rate performance of the $NiMoO_4$@3DGF and conventional $NiMoO_4$ nanowires electrodes, we tested the rate performance at various current densities ranging from 200 to 3200 mA g^{-1}, which are shown in Fig. 5d. All specific reversible capacity results of the $NiMoO_4$@3DGF electrode fall moderately with increasing current density, and the composite electrode capacity is higher than that of the $NiMoO_4$ nanowires electrode in each sweep speed. Even when the current density was as high as 3200 mA g^{-1}, a capacity of around 770 mA h g^{-1} was still available, which is higher than the theoretical capacity of the graphite anode of 372 mA h g^{-1}. More importantly, after the high rate discharge-charge cycles, a discharge capacity of about 915 mA h g^{-1} could be resumed and maintained for another 10 cycles without obvious decay when the current density was 200 mA g^{-1} again. The superior rate capability of the $NiMoO_4$@3DGF electrode is mainly attributed to the direct coupling of the active material onto the current collector thereby greatly enhancing the charge transfer properties. However, for the conventional $NiMoO_4$ nanowires electrode, an obvious drop in capacity is observed from the rate capability curve. This finding also corroborates the enhanced charge transfer obtained by direct coupling of $NiMoO_4$ nanowires on the 3DGF with highly electrical conductivity.

To further understand the electrochemical performance characteristics, we resorted to electrochemical impedance spectra (EIS) carried out at open circuit potential with an ac voltage of 5 mV amplitude in the frequency range from 100 kHz to 0.01 Hz. Fig. 6

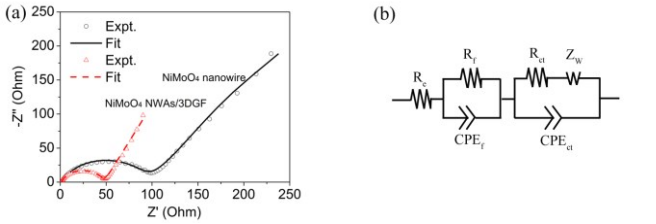

Fig. 6 (a) Original and fitted Nyquist plots of conventional $NiMoO_4$ nanowires and $NiMoO_4$ NWAs/3DGF electrodes， and (b) the corresponding equivalent circuit.

shows the Nyquist plots of the $NiMoO_4$ NWAs/3DGF and conventional $NiMoO_4$ nanowires electrodes and the fitted equivalent circuit. As shown in Fig. 6a, the Nyquist plots consist of one depressed semicircle at high-medium frequency and a slopping line at low frequency. The EIS data were fitted based on an equivalent circuit model consisting of ohmic resistance of the electrolyte and cell components (R_e), SEI layer resistance (R_f), dielectric relaxationcapacitance (CPE_f), charge-transfer resistance at the interface between the electrode and electrolyte (R_{ct}), double-layer capacitance (CPE_{ct}), and Warburg diffusion impedance (Z_w), and the result is shown in Fig. 6a.[55,56] The observed single semicircle is related to the combination of the surface film and charge-transfer resistance $R_{(f+ct)}$.[57,58] The fitted results reveal that the $NiMoO_4$ NWAs/3DGF electrode shows a much smaller $R_{(f+ct)}$ (48.36 Ω) as compared to that of the $NiMoO_4$ nanowires electrode (99.46 Ω). suggesting that the nanosheets possess a more stable surface film (including the SEI layer) and faster charge-transfer process. To recap, the results clearly demonstrate that the $NiMoO_4$ NWAs/3DGF electrode display favorable charge-transfer kinetics and much faster electron transport, and thus exhibit the dramatically enhanced lithium storage performance.

We believe that these excellent electrochemical performances can be attributed to the rationally designed nanoarchitecture of the $NiMoO_4$ NWAs/3DGF composites. Firstly, the nanowire arrays grow directly on conductive substrates to form integrated electrode, which is regarded as beneficial to improve the electric connection between the active material and current collector, and reduce the "dead volume" and resistance possibly caused by the polymer binder. Secondly, the 3D macroporous graphene networks with high conductivity and high specific surface area are served as a double highway for electron transfer and electrolyte ions to access into the electrode interior easily, which contribute to the much improved reversible capacities and rate capabilities. Thirdly, the open space between nanowires provides large electrolyte/electrode contact area and effective electrolyte-accessible channels for ion transportation, and shortens the distance for lithium ion diffusion,which is beneficial to enhance the reaction kinetics of electrode at different rates. Therefore, the as-prepared $NiMoO_4$ nanowire arrays supported on 3DGF present a promising high performance anode system for advanced lithium-ion batteries.

Conclusions

In summary, self-supported $NiMoO_4$ nanowire arrays have been grown on 3D conductive graphene foams through a facile hydrothermal route together with a post-annealing treatment. These self-supported, additive-free, unique $NiMoO_4$ NWAs/3DGF composites exhibits enhanced electrochemical cycling stability and rate capability compared to the conventional $NiMoO_4$ nanowires electrode. The dramatic improvement in the LIBs performance can be ascribed to the advantages endowed by the well-ordered nanowire arrays grown directly onto the surface of macroporous graphene foams, such as good contact of the active materials, tight adhesion with 3D macroporous graphene foams, large interfacial area for lithium insertion/extraction, and reduced ion diffusion pathways.

Acknowledgements

This work was financially supported by the National Natural Science Foundation of China (Grant No. 51271012) and Innovation Foundation of Beihang University for PhD Graduates. The authors thank the Analysis and Testing Center of the School of Materials Science and Engineering of Beihang University for support.

Notes and references

1 A. S. Arico, P. Bruce, B. Scrosati, J. M. Tarascon, and W. Van Schalkwijk, *Nat. Mater.*, 2005, **4,** 366.
2 K. S. Kang, Y. S. Meng, J. Breger, C. P. Grey, and G. Ceder, *Science*, 2006, **311,** 977.
3 L. Pan, X. -D. Zhu, X. -M. Xie, and Y. -T. Liu, *Adv. Funct. Mater.*, 2015, **25,** 3341.
4 W. Y. Zhang, Y. Zeng, N. Xiao, H. H. Hng, and Q. Y. Yan, *J. Mater. Chem.*, 2012, **22,** 8455.
5 L. Xiao, D. Q. Wu, S. Han, Y. S. Huang, S. Li, M. Z. He, F. Zhang, and X. L. Feng, *ACS Appl. Mater. Interfaces.*, 2013, **5,** 3764.
6 Y. Xiao, J. Zai, L. Tao, B. Li, Q. Han, C. Yu, and X. Qian, *Phys. Chem. Chem. Phys.*, 2013, **15,** 3939.
7 X. Hou, X. Wang, B. Liu, Q. Wang, T. Luo, D. Chen, and G. Shen, *Nanoscale*, 2014, **6,** 8858.
8 C. Wu, J. Maier, and Y. Yu, *Adv. Funct. Mater.*, 2015, **25,** 3488.
9 Y. Yao, S. Gong, P. Yang, Y. Xiao, K. Zhang, G. Keyshar, S. Ye, R. V. Ozden, and P. M. Ajayan, *ACS Appl. Mater. Interfaces.*, 2014, **6,** 20414.
10 J. Haetge, I. Djerdj, and T. Brezesinski, *Chem. Commun.*, 2012, **48,** 6726.
11 K. -S. Park, S. -D. Seo, H. -W. Shim, and D. -W. Kim, *Nanoscale Res. Lett.*, 2012, **7,** 35.
12 Q. Zhang, Y. Deng, Z. Hu, Y. Liu, M. Yao, and P. Liu, *Phys. Chem. Chem. Phys.*, 2014, **16,** 23451.
13 M. Mandal, D. Ghosh, S. Giri, I. Shakir, and C. K. Das, *RSC Adv.*, 2014, **4,** 30832.

14 C. T. Cherian, M. V. Reddy, S. C. Haur, and B. V. R. Chowdari, *ACS Appl. Mater. Interfaces*., 2013, **5,** 918.
15 N. N. Leyzerovich, K. G. Bramnik, T. Buhrmester, H. Ehrenberg, and H. Fuess, *J. Power Sources*, 2004, **127,** 76.
16 H. Yu, C. Guan, X. Rui, B. Ouyang, B. Yadian, Y. Huang, H. Zhang, H. E. Hoster, H. J. Fan, and Q. Yan, *Nanoscale*, 2014, **6,** 10556.
17 B. Wang, S. M. Li, X. Y. Wu, B. Li, J. H. Liu, and M. Yu, *Phys. Chem. Chem. Phys.*, 2015, **17,** 21476.
18 M. H. Seo, M. Park, K. T. Lee, K. Kim, J. Kim, and J. Cho, *Energy Environ. Sci.*, 2011, **4,** 425.
19 E. Lyyamperumal, S. Y. Wang, and L. M. Dai, *ACS Nano*, 2012, **6,** 5259.
20 Y. S. Luo, J. Jiang, W. W. Zhou, H. P. Yang, J. S. Luo, X. Y. Qi, H. Zhang, D. Y. W. Yu, C. M. Li, and T. Yu, *J. Mater. Chem.*, 2012, **22,** 8634.
21 J. P. Liu, J. Jiang, C. W. Cheng, H. X. Li, J. X. Zhang, H. Gong, and H. J. Fan, *Adv. Mater.*, 2011, **23,** 2076.
22 S. Sim, P. Oh, S. Park, and J. Cho, *Adv. Mater.*, 2013, **25,** 4498.
23 Y. G. Li, B. Tan, and Y. Y. Wu, *Nano Lett.*, 2008, **8,** 265.
24 Z. Chen, W. Ren, L. Gao, B. Liu, S. Pei, and H. M. Cheng, *Nat. Mater.*, 2011, **10,** 424.
25 H. Ji, L. Zhang, M. T. Pettes, H. Li, S. Chen, L. Shi, R. Piner, and R. S. Ruoff, *Nano Lett.*, 2012, **12,** 2446.
26 X. Wang, Y. Zhang, C. Zhi, X. Wang, D. Tang, Y. Xu, Q. Weng, X. Jiang, M. Mitome, D. Golberg, and Y. Bando, *Nat. Commun.*, 2013, **4,** 2905.
27 X. H. Cao, Z. Y. Yin, and H. Zhang, *Energy Environ. Sci.*, 2014, **7,** 1850.
28 X. Li, W. Cai, J. An, S. Kim, J. Nah, D. Yang, R. Piner, A. Velamakanni, I. Jung, E. Tutuc, S. K. Banerjee, and L. Colombo, R. S. Ruoff, *Science* 2009, **324,** 1312.
29 K. S. Kim, Y. Zhao, H. Jang, S. Y. Lee, J. M. Kim, K. S. Kim, J.-H. Ahn, P. Kim, J.-Y. Choi, and B. H. Hong, *Nature* 2009, **457,** 706.
30 H. Wang, H. S. Casalongue, Y. Liang, and H. Dai, *J. Am. Chem. Soc.* 2010, **132,** 7472.
31 P. Si, X. -C. Dong, P. Chen, and D. -H. Kim, *J. Mater. Chem. B.*, 2013, **1,** 110.
32 X. -C. Dong, H. Xu, X. -W. Wang, Y. -X. Huang, M. B. Chan-Park, H. Zhang, L. -H. Wang, W. Huang, and P. Chen, *ACS Nano*, 2012, **6,** 3206.
33 J. S. Luo, J. L. Liu, Z. Y. Zeng, C. F. Ng, L. J. Ma, H. Zhang, J. Y. Lin, Z. X. Shen, and H. J. Fan, *Nano Lett.*, 2013, **13,** 6136.
34 D. Guo, Y. Z. Luo, X. Z. Yu, Q. H. Li, and T. H. Wang, *Nano Energy*., 2014, **8,** 174.
35 D. Guo, P. Zhang, H. M. Zhang, X. Z. Yu, J. Zhu, Q. H. Li, T. H. Wang, *J. Mater. Chem. A.*, 2013, **1,** 9024.
36 S. E. Moosavifard, J. Shamsi, S. Fani, and S. Kadkhodazade, *RSC Adv.*, 2014, **4,** 52555.
37 L. Q. Mai, F. Yang, Y. L. Zhao, X. Xu, L. Xu, and Y. Z. Luo, *Nat. Commun.*, 2011, **2,** 381.
38 M. Niederberger, and H. Colfen, *Phys. Chem. Chem. Phys.* 2006, **8,** 3271.
39 X. Yu, B. Lu, and Z. Xu, *Adv. Mater.*, 2014, **26,** 1044.
40 D. Ghosh, S. Giri, and C. K. Das, *Nanoscale*, 2013, **5,** 10428.
41 X. F. Xia, W. Lei, Q. L. Hao, W. J. Wang, and X. Wang, *Electrochim. Acta*, 2013, **99,** 253.
42 K. B. Xu, J. Chao, W. Y. Li, Q. Liu, Z. J. Wang, X. J. Liu, R. J. Zou, and J. Q. Hu, *RSC Adv.*, 2014, **4,** 34307.
43 W. Hong, J. Q. Wang, P. W. Gong, J. F. Sun, L. Y. Niu, Z. G. Yang, Z. F. Wang, and S. R. Yang, *J. Power Sources*, 2014, **270,** 516.
44 J. Yan, Z. J. Fan, W. Sun, G. Q. Ning, T. Wei, Q. Zhang, R. F. Zhang, L. J. Zhi, and F. Wei, *Adv. Funct. Mater.*, 2012, **22,** 2632.
45 W. B. Yue, S. H. Jiang, W. J. Huang, Z. Q. Gao, J. Li, Y. Ren, X. H. Zhao, and X. J. Yang, *J. Mater. Chem. A.*, 2013, **1,** 6928.
46 X.Y. Wu, J. Du, H.B. Li, M.F. Zhang, B.J. Xi, H. Fan, Y.C. Zhu, Y.T. Qian, *J. Solid State Chem.*, 2007, **180,** 3288.
47 J. F. Marco, J. R. Gancedo, M. Gracia, J. L. Gautier, E. Rios, and F. J. Berry, *J. Solid State Chem.*, 2000, **153,** 74.
48 L. Zhou, D. Zhao, and X. W. Lou, *Adv. Mater.*, 2012, **24,** 745.
49 L. Zhang, H. B. Wu, and X. W. D. Lou, *Adv. Energy Mater.*, 2014, **4,** 1300958.
50 J. Lin, A-R. O. Raji, K. W. Nan, Z. W. Peng, Z. Yan, E. L. G. Samuel, D. Natelson, and J. M. Tour, *Adv. Funct. Mater.*, 2013, 24, 2044.
51 S. Kim, S. Ogura, H. Ikuta, Y. Uchimoto, and M. Wakihara, *Solid State Ionics*., 2002, **146,** 249.
52 S. Chattopadhyay, A. L. Lipson, H. J. Karmel, J. D. Emery, T. T. Fister, P. A. Fenter, M. C. Hersam, and M. J. Bedzyk, *Chem. Mater.*, 2012, **24,** 3038.
53 S. Laruelle, S. Grugeon, P. Poizot, M. Dollé, L. Dupont, and J. M. Tarascon, *J. Electrochem. Soc.*, 2002, **149,** A627.
54 K. Xiao, L. Xia, G. X. Liu, S. Q. Wang, L. -X. Ding, and H. H. Wang, *J. Mater. Chem. A*, 2015, **3,** 6128.
55 G. Wang, Z.Y. Liu, and P. Liu, *Electrochim. Acta*, 2011, **56,** 9515.
56 S. M. Li, B. Wang, J. H. Liu, and M. Yu, *Electrochim. Acta*, 2014, **129,** 33.
57 M. V. Reddy, T. Yu, C. H. Sow, Z. X. Shen, C. T. Lim, G. V. S. Rao and B. V. Chowdari, *Adv. Funct. Mater.*, 2007, **17,** 2792.
58 Y. Q. Zhu, C. B. Cao, J. T. Zhang, and X. Y. Xu, *J. Mater. Chem. A.*, 2015, **3,** 9556.

